Testing Core Loss for Rectangular Waveforms, Phase II Final Report

21 September 2011

Charles R. Sullivan
John H. Harris
Thayer School of Engineering at Dartmouth
charles.r.sullivan@dartmouth.edu
http://engineering.dartmouth.edu/inductor
8000 Cummings Hall
Hanover, NH 03755, USA

Sponsored by
The Power Sources Manufacturers Association
email: power@psma.com
http://www.psma.com/
P.O. Box 418
Mendham, NJ 07945-0418
Tel: (973) 543-9660
Fax: (973) 543-6207

Testing Core Loss for Rectangular Waveforms, Phase II Final Report

Charles R. Sullivan, John H. Harris
Thayer School of Engineering at Dartmouth
charles.r.sullivan@dartmouth.edu
http://engineering.dartmouth.edu/inductor
8000 Cummings Hall, Hanover, NH 03755, USA

21 September 2011

Summary

The Switching Power Converter Core Loss Project, Phase II is a follow-on to the Switching Power Converter Core Loss Pilot Project, conducted in 2009 [1]. In Phase II, we have accomplished these additional objectives:

- Gathered data on many more materials, particularly ferrites, and further validated the composite waveform hypothesis. More than 4000 experimental runs were performed.
- We confirmed that core losses per cycle increase when the voltage waveform includes off-time. This phenomenon was first noted in the Phase I project. Additional testing established that it is a real phenomenon, and not an artifact of the testing procedure. We also developed an alternative waveform that does not exhibit this behavior.
- Measurements were performed with a drilled core having embedding sense windings, looking for transient flux migration that might help explain off-time core loss.
- We developed a Steinmetz-like curve fit, and applied it to all the core characterization data. For the first time, a formula is available to predict loss accurately over a wide frequency range, avoiding glitches between frequency ranges that occur with other models. Furthermore, the model directly predicts loss with rectangular waveforms. It is available in different forms for different applications.
- We investigated the possibility of accidental residual magnetization biasing measurement results. We developed an automatic degaussing technique, and by comparing with previous results, we did not discover any evidence that the Phase I results were affected by such spurious magnetization.

There are four appendices to this report. In Appendix A, we illustrate that core loss of non-sinusoidal waveforms cannot be accurately predicted by separately examining the Fourier components of the waveform. In Appendix B, we provide an example of the use of the composite waveform model in a design application. In Appendix C we provide additional data plots. And in Appendix E we provide a a table with additional details of the Steinmetz-like loss modeling.

All of the data collected for this project accompany this report and are available for use by anyone. Full data from more than 4000 experimental runs are archived. For information about using the data generated in the project, see *Using the PSMA Rectangular Waveform Core Loss Data* [2].

Contents

1 Introduction **1**

2 The Basic Experiment **1**

3 Broader Data Set **4**

4 Drilled Core Experiments **4**
4.1 Geometry 4
4.2 Experimental Setup 6
4.3 Observations 7

5 Steinmetz Curve Fits **11**
5.1 Model in Terms of Pulse Width and Voltage 14

6 Dead-Time Loss **14**
6.1 Measurement Artifacts 14
6.2 Zero-Flux Off Time 16
6.3 An Improved "Predicted" Model 17
6.4 Conclusion 18

7 Degaussing **18**

8 Using the Data **20**

9 Future Work **20**
9.1 Modeling 21
9.2 Hardware 21
9.3 Flux Spatial Dynamics 22
9.4 Design Implications 22

10 Conclusion **22**

Appendices

A Steinmetz Harmonic Analysis **24**

B Example Application **26**
B.1 Conventional Parameters 26
B.2 Pulse width and Voltage as Parameters 28

C Characterization Plots **29**
C.1 Conventional Core Loss Plots 29
C.2 Herbert Curves 30
C.3 Hysteresis Plots 31

D Expand Plots **32**

E Extended Steinmetz Table **36**

List of Tables

1 Cores tested in the project. 5
2 Two-plane Steinmetz parameters 13
3 Published Steinmetz parameters 25
4 Example design parameters. 26
5 Calculated square-wave loss. 27
6 More two-plane Steinmetz parameters 37

List of Figures

1 Full-bridge excitation circuit. 2
2 Block diagram of the experimental apparatus. 3
3 Excitation waveforms. 3
4 Toroidal core with added constriction. 4
5 Drilled core and the subsection grid. 5
6 Flux distribution between subsections. 7
7 Flux distribution, showing a transient disturbance. 8
8 Central annulus flux distribution. 8
9 Flux migration 9
10 Raw oscilloscope data plot 10
11 Two-plane Steinmetz curve fit 12
12 `expand` waveform core loss vs. off time 15
13 `asym` waveform core loss vs. asymmetry 15
14 `skew` core loss vs. t_0 16
15 `hippo` waveform loss vs. off time. 17
16 Example design voltage waveform 27
17 Herbert plot for Ferroxcube 3C81 30
18 Hysteresis plot for Ferroxcube 3C81 31
19 `expand` core loss vs. off-time for Ceramic Magnetics MN60. . . . 32
20 `expand` core loss vs. off-time for Ceramic Magnetics MN8CX. . . 32
21 `expand` core loss vs. off-time for Ferroxcube 3C81. 33
22 `expand` core loss vs. off-time for Ferroxcube 3C90. 33
23 `expand` core loss vs. off-time for Ferroxcube 3F3. 33
24 `expand` core loss vs. off-time for Magnetics F. 34
25 `expand` core loss vs. off-time for Magnetics K. 34
26 `expand` core loss vs. off-time for Magnetics L. 34
27 `expand` core loss vs. off-time for Magnetics P. 35
28 `expand` core loss vs. off-time for Magnetics R. 35
29 `expand` core loss vs. off-time for Magnetics W. 35

1 Introduction

In the design of magnetics for switching power applications, it is essential to accurately estimate core loss, but current methods based on sinusoidal data are difficult to use and inaccurate. Phase I of this project established the feasibility and value of a new method proposed by Herbert [3], in which a simplified set of square-wave measurements produces data that can be used to calculate loss for *any* alternating rectangular-voltage waveform.

The hypothesis to be tested was that, for alternating rectangular pulses and a given magnetic core material, the core loss energy per period depends only on component pulse widths and peak voltages. We call this the *composite waveform hypothesis* (CWH).

In Phase I of the program, we established that this hypothesis, while not perfect, works well enough to be a significant improvement in both accuracy and ease of use, compared with methods based on sinusoidal data. It is convenient to decompose rectangular waveforms into such pulses for analysis. Thus, it is sufficient to test cores with square voltage waveforms, and then use the data to predict losses with generalized rectangular voltage waveforms.

Phase II of the project addresses these additional objectives:

1. To gather more square wave data to characterize additional core materials and geometries, as well as validation data, to further test the CWH.
2. To investigate the dynamics of core flux distribution using embedded sense windings.
3. To provide Steinmetz or similar curve-fitting parameters, for use in numerical design techniques.
4. To investigate the anomalous results discovered in Phase I involving prolonged off-time waveforms.
5. To investigate the possibility of experimental error due to residual magnetization in sample cores.
6. To demonstrate the use to this methodology in a design application.
7. To demonstrate the shortcomings of core loss estimates obtained by summing sinusoidal Steinmetz estimates for rectangular waveform harmonics.
8. To improve data management and presentation to make the results more accessible to users.

In the sections that follow, we discuss the topics listed above in detail.

2 The Basic Experiment

In the basic experiment, a magnetic core is driven with a full bridge switching circuit (Figure 1). There is a second sense winding for measuring flux, to avoid

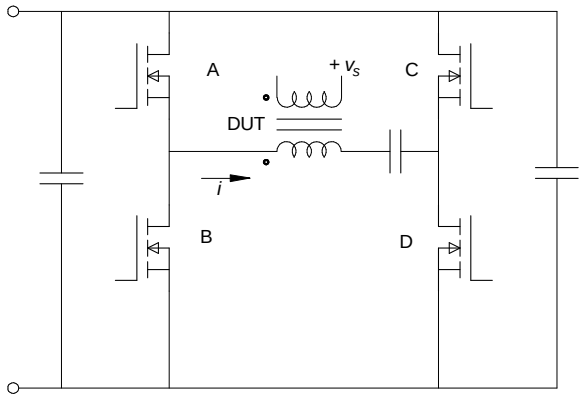

Figure 1: Full-bridge excitation circuit. The device under test (DUT) is a magnetic core.

measuring resistive loss in the drive winding. A blocking capacitor insures zero net DC current. In most tests, the capacitor voltage is negligible, and is only needed to cancel small volt-second mismatched due to timing errors. However, asymmetric waveforms are implemented by using significantly different on-times for positive and negative pulses. The capacitor voltage automatically adjusts to reduce the voltage of the longer pulse in order to have equal volt seconds between positive and negative pulses. Our apparatus is capable of taking measurements in a range of about 5 kHz to 500 kHz. The sample core is oil cooled, usually kept at 80 °C.

We take measurements with an Agilent Technologies DSO 7104A oscilloscope. Current is measured with a Tektronix P 6021 AC current probe. The switching bridge is controlled by a programmable function generator with some additional logic. This determines the frequency and pulse lengths. The bridge power supply voltage determines the voltage amplitude. All three instruments are under the control of a computer, which orchestrates sets of experiments and manages the resulting data (Figure 2). The oscilloscope sweep time is one period. It averages the information from 512 triggers, and saves voltage and current information at 1000 time-points per period.

We refer to one of these experiment as a *run*—think of a run as single captured waveform. A run takes only a few seconds, but wound cores are normally tested with a batch of runs, called a *run set*, in which frequency, amplitude, and pulse widths are varied from run to run. Run sets always include square wave runs, which characterize the coil under test. Data from more than 4000 runs have been collected and accompany this report. Other wave forms (Figure 3) are also usually included to provide validation of the CWH, or for exploring other phenomena.

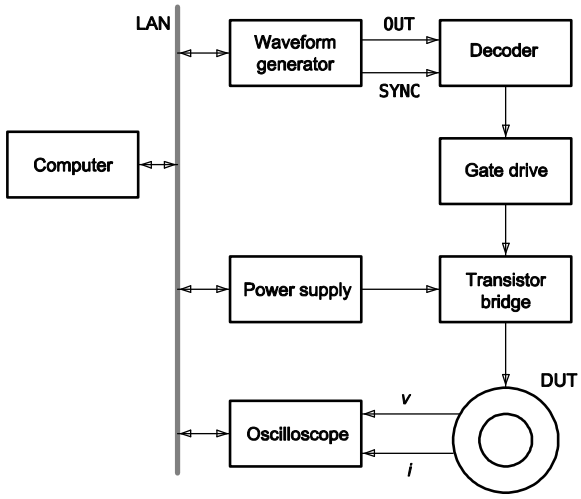

Figure 2: Block diagram of the experimental apparatus. The power supply, drive bridge, and oscilloscope are all controlled by the computer, which also gathers, and analyzes, the resulting data.

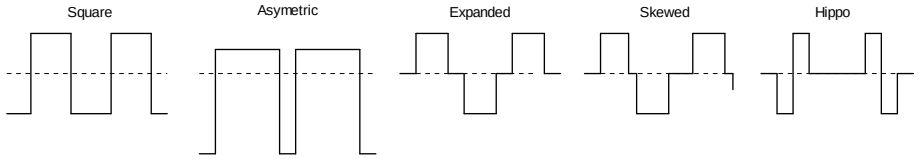

Figure 3: Excitation waveforms. The `hippo` waveform was added in Phase II, and was found to avoid the loss increase observed in the `expand` waveform.

3 Broader Data Set

We have tested and provide test data for twenty different wound samples, including eleven different materials from four different manufacturers. These are summarized in Table 1.

Most of the cores are toroidal, but to test the effect of varying cross-section area and corners, the selection includes E-cores. In another test of the effect of flux constriction, we ground a flat side on a toroidal core (Figure 4). The E cores and flattened-toroidal cores showed the same general behavior and characteristics as the toroidal cores, although the specific loss values were affected.

To search for anomalous behavior we examined over 400 files. We noted no significant qualitative difference with regard to the CWH in the results—it holds for this broader select of cores. There may be effects of the corners and constrictions that we did not discover in this evaluation, and we encourage continued examination and analysis of the data to potentially uncover additional phenomena of interest.

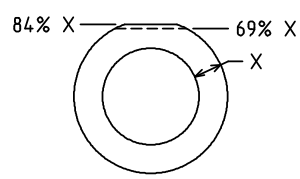

Figure 4: Toroidal core with added constriction. The same core was tested with no constriction (run set `mi01-1`), and with the cross section area reduced to 84% (`mi009`), and 69% (`mi010`) of the total, by grinding a flat section.

4 Drilled Core Experiments

We investigated core flux distribution using a ferrite core with embedded sense windings. A core was fabricated with four holes drilled through—two intersecting pairs, forming two *cross points* (Figure 5, left). One hole of a pair is radial, perpendicular to the axes of the toroid, the other is parallel to it. Each cross point divides the cross section into unequal quadrants. By threading wires through the holes, we can form a single-turn sense winding to measure the flux in any quadrant, or any adjacent pair of quadrants. By subtracting the signal from different wirings, we can infer the flux in any of the nine subsections.

4.1 Geometry

The drilled core was fabricated from a toroidal core having a square cross-section, $0.5 \times 0.5\,\mathrm{in}^2$ (a Magnetics Div., Spang & Co. Inc. 0F46113TC). The two cross points were chosen to collectively divide the core area into nine equal, square subsections. The two pairs of holes are displaced circumferentially about

Manufacturer Material	Shape	Core ID
Ceramic Magnetics Inc		
MN60	23.2,14.5,7.2T	cm01
MN8CX	23.2,15.1,7.7T	cm02
Ferroxcube		
3C81	E19/8/5	fx09
3C81	TX22/14/13	fx003
3C90	TX22/14/6.4	fx010
3F3	E19/8/5	fx05
3F3	TX22/14/13	fx004
Magnetics Inc.		
F	42206-TC	mi005
F	46113-TC	mi11-1
K	42206	mi007
L	2206	mi08
P	42206-TC	mi003
R	42206-TC	mi001
R	custom	mi009
W	42206	mi02
Payton Tech.		
amorph. Co	18x11x10	pt01

Table 1: Cores tested in the project.

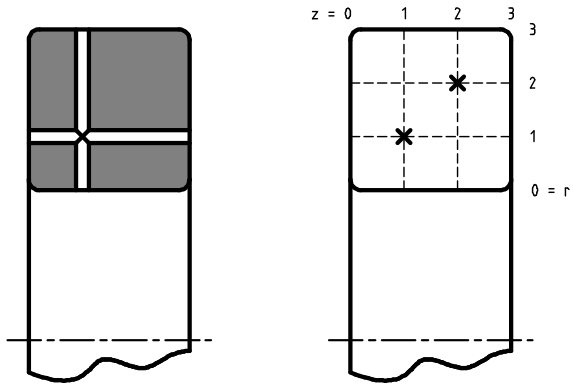

Figure 5: Section view of a drilled core showing one pair of cross-point holes (left), and the grid used to describe subsection geometry (right). Cross points are show with an $\times$.

the toroid, to avoid unnecessary constriction of the flux path due to the holes. (The drawing is to scale; a single cross-point pair consumes 15% of the core cross section area.) We take advantage of the symmetry of the toroid, and collapse the circumferential dimension, regarding the cross points as lying in one radial cross-section plane (Figure 5, right). The details of the naming of subsections, necessary for interpreting the data, are presented in the user manual [2].

4.2 Experimental Setup

For these runs, the voltage across the embedded sense winding was recorded on an additional oscilloscope channel. The core had $N = 4$ turns for the primary winding. By averaging over 512 triggers, the noise on the single-turn sense winding was typically below the resolution of the oscilloscope digitization. Unlike the routine runs, the center hole in the toroid was not blocked with a low-dielectric-constant material, in order to avoid fouling the probe holes. Measurements were made at room temperature. Automatic degaussing was used (Section 7).

The sample was driven with square wave signals, and with the `expand` validation waveform. Our objective was to detect any unusual dynamic variation of the fraction of flux passing through the subsection, under these various drive conditions. We generated plots of three values: (1) the full-core sense winding voltage, (2) the embedded winding voltage, and (3) the ratio of the two (Figure 6). To make visual comparison easier, the embedded winding voltage was scaled by NA/A_p, where N is the number of turns around the full cross-section, A is the full core cross-section area, and A_p is the "probe area," the area of the core enclosed within the sense winding. This ratio would be unity if the flux distribution were uniform.

Even under the null hypothesis that there are no new dynamic flux distribution effects discovered, and that the permeability is constant, uniform and isotropic, we would not expect the flux distribution be uniform—there is a radial gradient, with $B \propto 1/r$. The flux contained in the annulus between r_1 and r_2,

$$\Phi(r_1, r_2) = h \int_{r_2}^{r_1} B(r) dr \quad (1)$$

$$\propto \log(r_1) - \log(r_2) \quad (2)$$

and h is the height of the toroid. For our drilled core,[1] this leads us to expect (under the null hypothesis) ratios of 119%, 98.1%, and 83.4%, in that order, from inside out. The ratio in Figure 6 averages 116%.

Also, of the nine subsections, the four corner subsections have slightly less area, due to the corner radii, and will enclose less flux. The manufacturer does not specify this radius, and we did not measure it, being more interested in the dynamics of the flux distribution.

[1] Using the manufacturer's nominal dimensions.

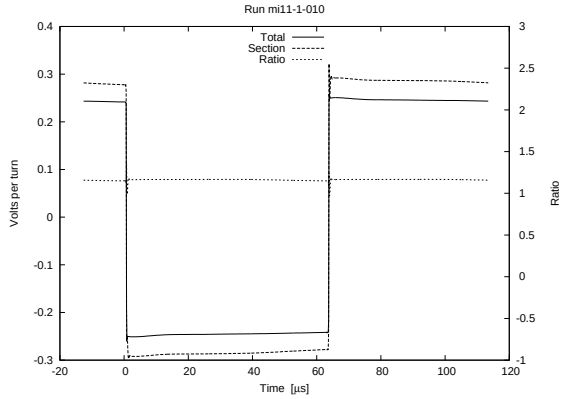

Figure 6: Flux distribution between subsections. The total flux is compared with the flux through the inner 1/3 annular section (designated 0031) of a toroidal core (the latter scaled by NA/A_p). The third plot is the ratio of the two.

4.3 Observations

We are looking for variations in the flux distribution with time, which should show up as deviations of the sense winding voltage ratios from a constant. Such deviations could be caused by changes in the flux distribution in the core, or by spurious artifacts of the measurement apparatus. Careful examination of the data can distinguish between the two.

In Figure 6 we see an interesting feature of the ratio plot—a transient at the zero crossings. Figure 7 shows this more clearly, because here the period is $8\,\mu$s, instead of $120\,\mu$s, and ringing at about 1.5 MHz is easily seen. This ringing appears in all the probe winding plots, but the outer, total-flux winding only shows the 30 MHz ringing characteristic of the drive circuitry. If the lower frequency ringing is due to flux migrating from one region to another, we expect this lower frequency ringing to sum to zero across regions, and the polarity of some regions to be reversed.

Figure 8 shows the central annulus with the same excitation voltage, and we see *inverted* low-frequency ringing. Figure 9 tells the whole story. In it, the probe winding voltages for all three annular layers of the core, and their sum,[2] are plotted together. The flux appears to move in and out of the central region from the other two regions. The lower frequency transients all cancel out in the sum of the three voltages, leaving only the high-frequency, drive circuit artifacts.

We believe the low frequency ringing is due to dimensional resonances, such as described in [4], and are evident because of the low electromagnetic propagation velocity (v) of the ferrite medium. Because v is low, resonances due

[2]This is the sum of the three probe voltages, *not* the outer sense winding voltage, scaled.

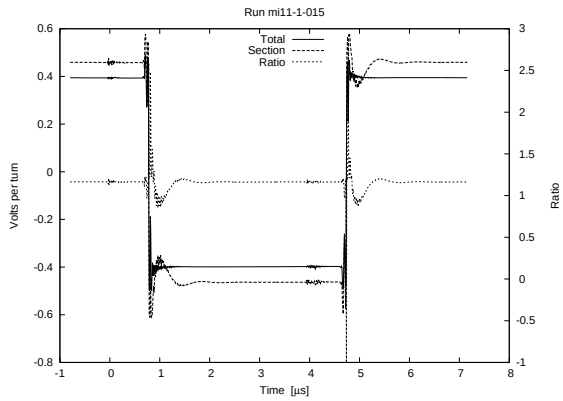

Figure 7: Flux distribution, showing a transient disturbance. This is the same subsection of the core as in Figure 6, but at a higher frequency. The disturbance could be a transient flux migration.

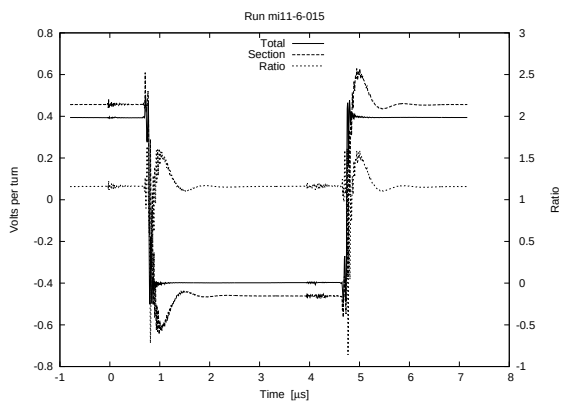

Figure 8: Central annulus flux distribution. This probe subsection is the central 1/3 annulus (designated 0132). The transient disturbance shows reversed polarity compared to Figure 7.

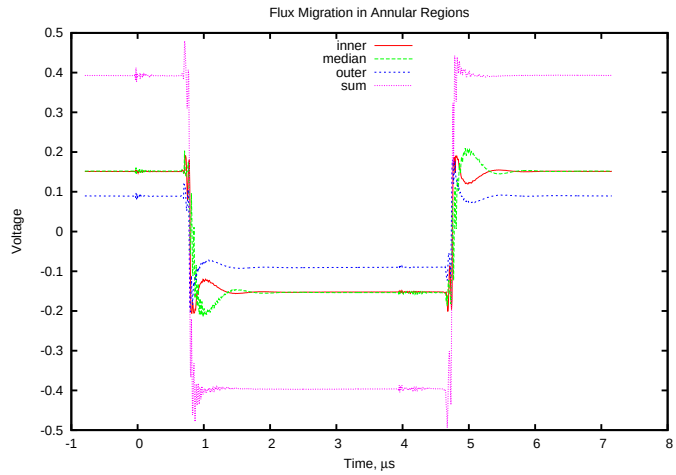

Figure 9: Flux migration is evident from probe winding voltages for the three disjoint annular regions of the drilled core. disturbance shows reversed polarity in the central region. The sum shows no low-frequency transient.

to the geometry of the core can have frequencies within the band of interest. It is perhaps counterintuitive that v could be so low that this effect would be significant for such a small device ($\sim 1\,\mathrm{cm}$) and modest bandwidth ($\sim 1\,\mathrm{MHz}$). Consider the familiar equation for propagation velocity,

$$v = \frac{c}{\sqrt{\mu_r \epsilon_r}}, \tag{3}$$

where c is the velocity of light in a vacuum, and μ_r and ϵ_r are the relative permeability and permittivity, respectively. We expect a large μ_r for a ferrite core, but ϵ_r is seldom published for ferrites, and so may be unfamiliar. Magnetics [5] gives a value of $\mu_r = 750$ for the F material used in these experiments, but does not publish a permittivity. However, Ferroxcube's catalog ([6], p.61) presents a table, for MnZn ferrites in general, of estimated ϵ as a function of f under sinusoidal excitation. It lists $\epsilon_r \approx 10^5$ at $1\,\mathrm{MHz}$.[3]

To see if dimensional resonance is a plausible explanation for the transient voltages we observe, we will try to estimate ϵ_r from our observations. Imagine an infinite cylindrical medium with a cross-section matching our toroid, driven by a step function at its boundaries. We would expect it to ring with a fundamental wavelength, λ, equal to twice its width ($2 \times 12.5\,\mathrm{mm}$). We have observed a ringing frequency, $f \approx 1.5\,\mathrm{MHz}$, so we can calculate $v = f\lambda$. Substituting this

[3] Inspecting the table, we see a strong dependence of ϵ_r on f—ferrite is a dispersive medium, and we are driving the core with square waves. We should regard this number as a rough approximation.

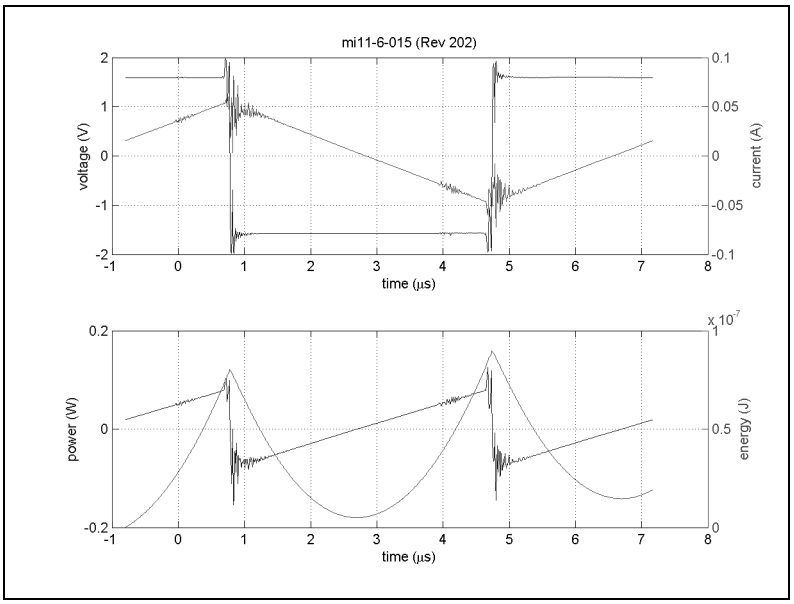

Figure 10: Raw oscilloscope data plot for the drilled core. The power and energy plots in this image could show losses due to the flux migration transient if they are significant. (The probe winding voltage does not appear in the standard oscilloscope plots.)

into (3) and solving for ϵ_r, we get

$$\epsilon_r = \frac{1}{\mu_r}\left(\frac{c}{f\lambda}\right)^2 \tag{4}$$

$$\approx \frac{1}{750}\left(\frac{3\cdot 10^8\,\mathrm{m/s}}{(1.5\,\mathrm{MHz})(25\,\mathrm{mm})}\right)^2 \tag{5}$$

$$\epsilon_r \approx 8.4\cdot 10^4. \tag{6}$$

This is close to the same order of magnitude as Ferroxcube's estimate for their similar materials, making the dimensional resonance theory look plausible, though further study is merited (Section 9.3).

One might wonder whether this flux migration causes significant loss. If so, it would appear in the oscilloscope data plot (Figure 10), and affect the current, power, and energy curves. The energy plot gives a particularly clear view, because the integration smoothes the drive circuit transient ringing. We see nothing unusual around the time of the flux migration (the first 1.5 μs of a pulse).

It is worth noting that the flux distribution transients, lasting scarcely 2 μs, are unlikely to explain the off-time loss phenomena described in Section 6.

The full data from these experiments accompanies this report, and is avail-

able for further investigation of possible flux migration phenomena.

5 Steinmetz Curve Fits

The Steinmetz[4] approximation,

$$\overline{P_v} = k f^{\alpha} \hat{B}^{\beta}, \tag{7}$$

where $\overline{P_v}$ is the average power density, f is the excitation frequency, and $\hat{B}$ is the peak flux density, is commonly used to characterize core loss data for sinusoidal excitation, but can also be applied to our square-wave data. We first describe a formulation in terms of frequency and flux density, but then also provide a formulation in terms of pulse widths and applied voltage.

To linearize the equation for curve fitting, we used base-10 logarithms (referenced to 1 V or 1 s), because the preferred values for voltage and time used in the experiment are round decilog values, and because using $\log_{10}$ makes it convenient to express the standard error in familiar units of decibels (i.e., $10 \log_{10}(P/P_{\text{ref}})$). This choice does not affect the values of the k, α, and β parameters.

In a typical case, Ferroxcube 3C81 material, fitting (7) to the entire set of square wave data gave a standard error of about 1.5 dB. Visually inspecting the plots shows a distinct increase in slope around 100 kHz. This inspired a six-parameter, two-plane curve fit,

$$\overline{P_v} = \max(k_1 f^{\alpha_1} \hat{B}^{\beta_1} + k_2 f^{\alpha_2} \hat{B}^{\beta_2}) \tag{8}$$

This fits the data to two intersecting planes that function like a single plane with a fold in it (Figure 11). It fits the 3C81 data with a standard error of 0.35 dB, much better than the single equation, and also better than simply using different parameters for different frequency ranges.

Note that while the formula we are fitting is essentially the same form as the Steinmetz equation, and we use the variable names k, α, and β, this is a *different* model, because is is based on square wave experimental data, and is intended to predict rectangular pulse core losses. In situations where this might cause confusion, we will subscript the present parameters[5] to distinguish them from the classic Steinmetz, sinusoidal, parameters.

The boundary between the two planes (the fold) projected onto the $\log_{10}(f)$-$\log_{10}(\hat{B})$ plane is a straight line,

$$\log_{10}(\hat{B}) = a_0 + a_1 \log_{10}(f) \tag{9}$$

where

$$a_0 = \frac{\log_{10}(k_1/k_2)}{\beta_2 - \beta_1}$$

[4] Named for C. P. Steinmetz's work [7], although Steinmetz did not include the frequency dependence that is now standard [8].

[5] We choose 'r', for "rectangular," thus avoiding 's' which might suggest either "square" or "sinusoidal."

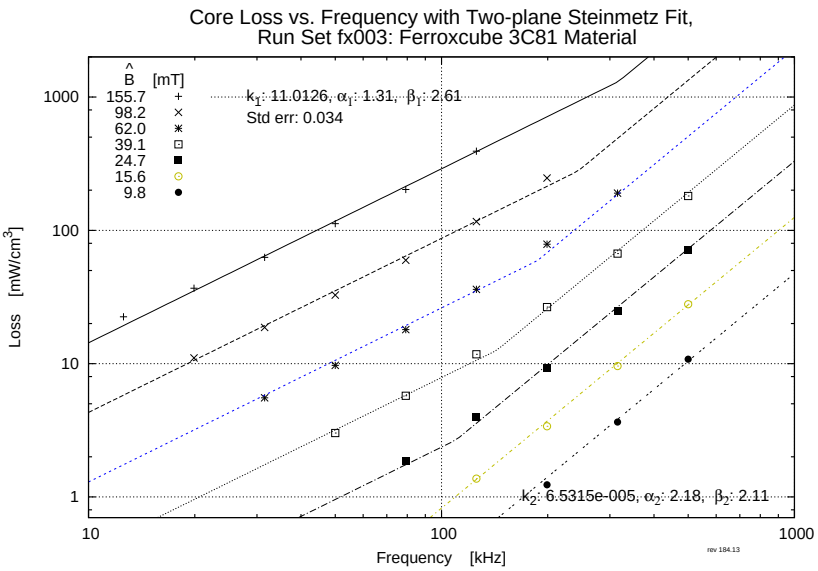

Figure 11: Two-plane Steinmetz curve fit to Ferroxcube 3C81 material, square wave loss data.

$$a_1 = \frac{\alpha_1 - \alpha_2}{\beta_2 - \beta_1}.$$

The parameters a_0 and a_1 might provide a useful characterization of the transition of the dominating loss mechanisms from hysteresis to eddy currents, for comparing different materials. The two-plane Steinmetz parameters from our experiments are listed in Table 2.

This method of curve fitting has advantages over the common practice of providing independent Steinmetz parameters for different frequency ranges:

1. There is no step discontinuity at frequency range boundaries.
2. There is no arbitrary choice of boundary frequency. The curve-fitting optimization chooses the best boundary line (i.e., choosing a_0 and a_1).
3. The curve fitting optimization uses *all* the data.

There is no significant computational penalty for using this model, and coding is easy; programmers can use either (8) directly, or (7), using k_1, α_1, and β_1 for $\log_{10}(\hat{B}) > a_0 + a_1 \log_{10}(f)$, and k_2, α_2, and β_2 otherwise.

The two-plane Steinmetz parameters from our experiments are listed in Table 2. The table includes two different sets of k values. The lowercase k_1 and k_2 are the values used in (8), implicitly using reference values of 1 T and 1 Hz. Also listed are uppercase K_1 and K_2 based on reference values $f_0 = 100\,\text{kHz}$

Manufacturer Material	Geom	Set	k_1	K_1	α_1	β_1	γ_1	k_2	K_2	α_2	β_2	γ_2
Ceramic Magnetics Inc												
MN60	T	cm01	6.085	86810	1.32	2.47	2.15	899.8μ	67879	2.00	2.13	1.13
MN8CX	T	cm02	63.01	182100	1.19	2.49	2.3	177.4μ	87357	2.20	2.29	1.09
Ferroxcube												
3C81	T	fx003	11.01	91200	1.31	2.61	2.3	65.32μ	41432	2.18	2.11	0.93
3C81	E	fx09	18.02	88800	1.23	2.45	2.22	350.0μ	52769	2.10	2.33	1.23
3C90	T	fx010	36.86	39570	1.19	2.94	2.75	2.895μ	18223	2.39	2.16	0.77
3F3	T	fx004	102.4	67200	1.13	2.81	2.68	11.93μ	28414	2.30	2.14	0.84
3F3	E	fx05	40.63	65950	1.14	2.50	2.36	224.8μ	38221	2.12	2.36	1.24
Magnetics Inc.												
F	T	mi005	26.41	72920	1.24	2.76	2.52	7.612μ	32369	2.37	2.22	0.85
K	T	mi007	246.2	86830	1.10	2.95	2.85	5.276μ	20750	2.41	2.48	1.07
L	T	mi08	706.8	150800	1.04	2.87	2.83	276.1m	99927	1.69	2.88	1.19
P	T	mi003	10.91	43090	1.28	2.80	2.52	75.99μ	36099	2.16	2.13	0.97
R	T	mi01-6	30.16	67220	1.25	2.90	2.65	14.55μ	30033	2.31	2.24	0.93
W	T	mi02	832.7m	131000	1.51	2.37	1.86	10.59m	123857	1.82	2.04	1.22

Table 2: Two-plane Steinmetz parameters for various magnetic materials in two general geometries, toroidal (T) and E-core (E). The k_i parameters are referenced to $f = 1\,\mathrm{Hz}$ and $\hat{B} = 1\,\mathrm{T}$; the K_i parameters are referenced to $f = 100\,\mathrm{kHz}$ and $\hat{B} = 100\,\mathrm{mT}$. All the k_i and K_i parameter have dimensions of $\mathrm{W/m^3}$. The α and β parameters for use in (8); γ is required for (11).

and $\hat{B}_0 = 100\,\mathrm{mT}$, to be used in

$$\overline{P_v} = \max\left(K_1(f/f_0)^{\alpha_1}(\hat{B}/\hat{B}_0)^{\beta_1} + K_2(f/f_0)^{\alpha_2}(\hat{B}/\hat{B}_0)^{\beta_2}\right) \tag{10}$$

Both are included because the (8) is simpler to use, but the values of K_1 and K_2 are more physically meaningful, because they are based on results near the range of values used in practice, rather than on values many orders of magnitude different.

For example, the values of K for one core shape are very similar to those for another core shape and the same material, indicating that the losses predicted by the model are very similar for the two shapes. The values of k, on the other hand, can be very different, but this is only an artifact of the use of the 1 T and 1 Hz reference points, which are distant from the actual operating point, and is not an indication that the predictions in the region of interest are significantly different.

The results tend to indicate slightly smaller losses for E cores than for toroidal cores made with the same material. This does not actually indicate of superior performance for E cores. Rather, it is a result the effective area and effective core length provided one the core datasheet, which we used in our calculations.

5.1 Model in Terms of Pulse Width and Voltage

The model (8) can be reformulated in terms of pulse width and voltage. For direct use with that composite with form hypothesis, we also reformulated it to represent the energy loss for one pulse, rather than the average power loss over a whole cycle. This results in energy loss per pulse, per unit volume, of

$$E_{v,a} = \max\left(\frac{k_1}{(NA)^{\beta_1} 2^{(\beta_1+\alpha_1)}} V_a^{\beta_1} t_a^{\gamma_1}\ ,\ \frac{k_2}{(NA)^{\beta_2} 2^{(\beta_2+\alpha_2)}} V_a^{\beta_2} t_a^{\gamma_2}\right) \tag{11}$$

where V_a is the voltage applied during a pulse of duration t_a, A is the cross-section area of the core, and N is the number of turns. The parameter γ is provided in Table 2, for convenience, but can also be simply calculated from α and β:

$$\gamma = 1 + \beta - \alpha. \tag{12}$$

The application of this formula is illustrated in Appendix B.

6 Dead-Time Loss

In Phase I, we discovered a significant deviation from the CWH during periods of prolonged constant flux. This was most evident with the `expand` waveform, in which a square wave is stretched by inserting off-time between the square pulses—thus increasing the period while holding the pulse widths constant. For example, in Figure 12 we plot loss versus off time, t_0. The "predicted" value is simply the loss measured for the characterization square-wave measurement. In contrast, the CWH works well for the asymmetric waveform (Figure 13), which has no dead time

The effect is also noticeable in plots of the `skew` waveform (Figure 14). The core loss is uniformly higher than for square waves, at about the same value as seen for the `expand` waveform having the same period. Unlike the `expand` waveform, the plot is not significantly slopped—the increased loss due to greater off time in one part of the waveform is about offset by the decreased loss due to lesser off time in the other part.

In Phase II, we want to determine if the phenomenon is real, and if so, possibly characterize it.

6.1 Measurement Artifacts

In order to check for possible errors introduced by the apparatus, we repeated a representative experiment with (1) a DC current probe, and (2) increased bridge blocking capacitance. Neither precaution made a significant difference.

The magnetization current is routinely measure using a Tektronix P6021 AC current probe (set to 10 mA/mV). For this experiment we substituted a Tektronix TCP303 current probe. As an extra precaution, we did the probe degaussing procedure before each run. (Run set `mi05-5`)

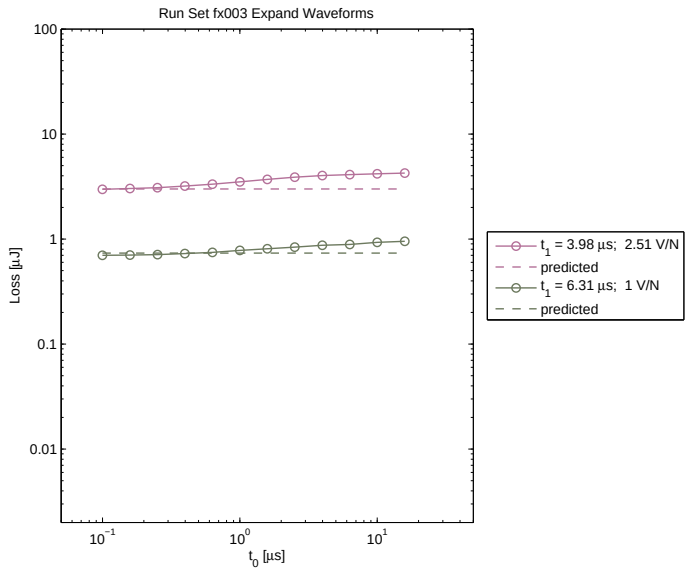

Figure 12: `expand` waveform core loss vs. off time between pulses. The "predicted" value is the loss measured for a square wave ($t_0 = 0$). Additional plots of this effect for different materials, are provided in Appendix C.

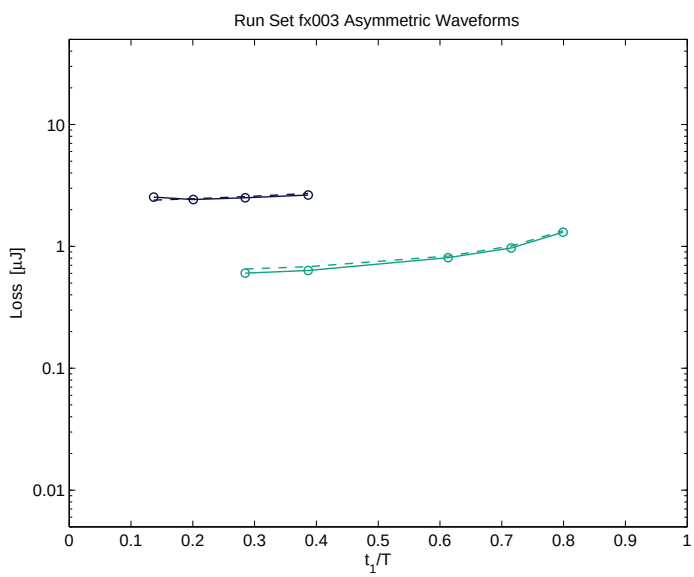

Figure 13: `asym` waveform core loss vs. asymmetry, t_1/T. The "predicted" value is the sum of the losses measured for square wave pulses of length t_1 and $T - t_1$.

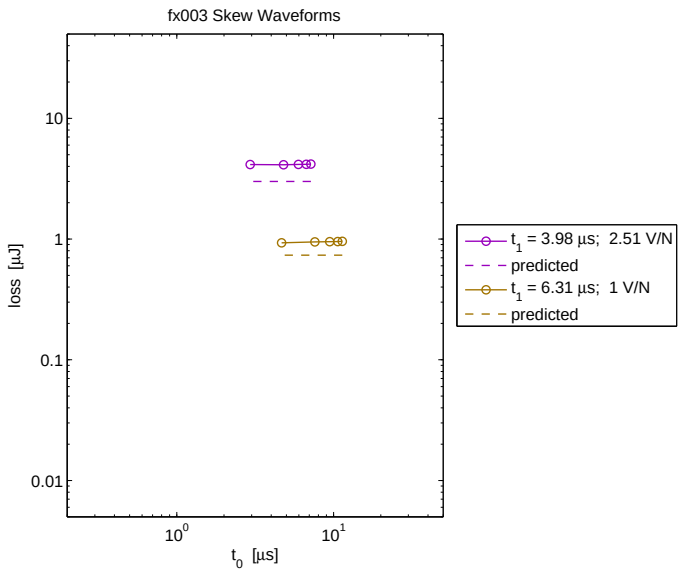

Figure 14: `skew` core loss vs. t_0, where t_0 is the off time between the first and second pulses. The other off time equals $T - 2t_1 - t_0$

.

In Phase I, the bridge was equipped with a 320 μF blocking capacitor. On very long `expand` runs, low-frequency ringing was evident. We wanted to improve this performance by increasing the blocking capacitance, while lowering the effective series resistance, so we installed 120 mF of blocking capacitance, using Epcos MKT series polyester capacitors.

6.2 Zero-Flux Off Time

In order to see if the extra loss is correlated with the presence of magnetic flux, we devised a new wave form, the *hippo* (Figure 3), named for its resemblance to hippopotamus dentition. This waveform has two pairs of pulses, with each *pair* having a width of t_1 (i.e., two opposing pulses of width $t_1/2$). Thus the flux returns to zero during the off time. Using this waveform, the measured loss matched the predicted value more closely, actually dropping somewhat (Figure 15). [6]

[6] We also note a curious hump in the plot at very low t_0. This is an artifact of the apparatus—the waveform decoder circuitry ([1], Section 4) has a delay of about 400 ns in the `OUT` signal rise time, making unable to create this short a dead time for the `hippo` waveform. The plot time scale is based on the `SYNC` signal, not the actual sense winding voltage.

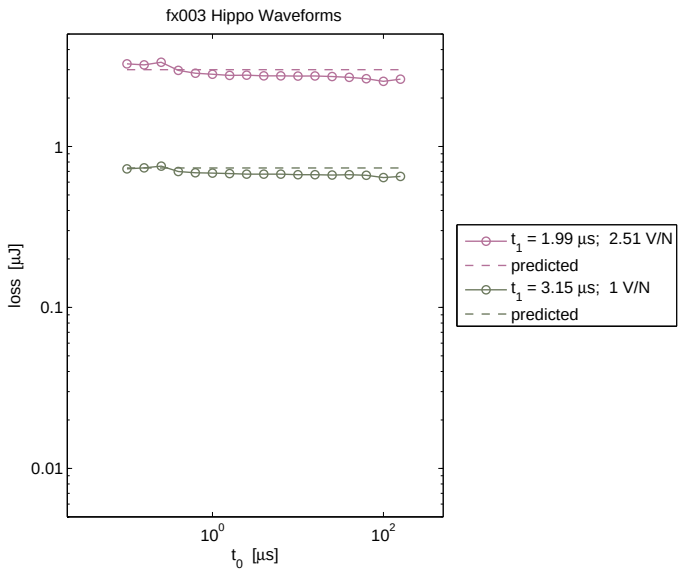

Figure 15: `hippo` waveform loss vs. off time.

6.3 An Improved "Predicted" Model

In Phase I, the "predicted" values were simply the square-wave values, taking the excitation voltage to be zero during the off time. This is not quite correct, since the power supply is merely disconnected from the device under test, instead of enforcing zero voltage across it. As a result, the iR drop across the winding causes the flux to droop during the off time—the excitation waveform has an approximately trapezoidal segment during this interval. We expect this change in flux to cause some core loss.

It is tempting to think this segment could be approximated by a square segment, and invoke the CWH, but the CWH applies only to waveforms composed of *alternating* rectangular pulses. When stepped pulses are allowed, the model becomes inconsistent; for example, it would imply that core loss is independent of frequency, as in the case of square wave pulses at frequency f, which could be considered to be composed of *pairs* of pulses of width $T/4$.

There is a piecewise linear (PWL) model presented by by Venkatachalam, et al [9], that *is* applicable. Their work is on a more general semiempirical model, but it predicts a PWL power density

$$P_D = \frac{k_i(\Delta B)^{\beta-\alpha}}{T} \sum_m \left| \frac{\Delta_m B}{\Delta_m t} \right|^{\alpha} \Delta_m t, \tag{13}$$

where ΔB is the peak-to-peak flux density for the overall waveform, and Δ_m indicates changes over the mth segment of the piecewise decomposition. The parameters α and β are the (sinusoidal) Steinmetz parameters, and k_i is their

own parameter, derived from the Steinmetz parameters.

For this application, k_i is derived from our rectangular-wave Steinmetz curve fit. We start with (13) for a square wave, i.e., $\Delta B = 2\hat{B}$ and $\Delta t = T/2$:

$$P_D = \frac{k_i (2\hat{B})^\beta}{T(2\hat{B})^\alpha} 2 \left(\frac{2\hat{B}}{T/2} \right)^\alpha \frac{T}{2}, \tag{14}$$

which reduces to

$$P_D = k_i 2^{\alpha+\beta} f^\alpha \hat{B}^\beta. \tag{15}$$

This very similar to one plane of (8), and if we equate them we find that

$$k_i = \frac{k_r}{2^{\alpha_r+\beta_r}}, \tag{16}$$

where k_r, α_r, and β_r are the rectangular-wave Steinmetz parameters.

There is still the interesting question of which plane of the two-plane curve fit to use, but in the example in the following discussion, all factors suggest the low-frequency plane is the best choice, and we will proceed with that.

This model is easy to apply to our data—after integration, the $B(t)$ data are quite clean, without evidence of ringing and switching transients. The waveform is crisp and easily decomposed into PWL segments. We will now consider a particular run, `fx003-90`, which uses a Ferroxcube 3C81 core, excited with 1.26 V/turn, 4 μs pulses, stretched to a period of 8 μs.

Model	Loss/cycle	Relative
Measured	4.243 μJ	147.4%
PWL predicted	2.918 μJ	101.4%
Simple predicted	2.879 μJ	100.0%

From this we see that the two different predictions—the simple prediction, and the corrected prediction developed in this section—differ only slightly. That means that our original conclusions are unaltered by this analysis: that is, that the off-time loss phenomenon is real. Specifically, in this case, it results in nearly a 50% increase in loss.

6.4 Conclusion

From these observations we conclude that there is indeed some loss mechanism having a long relaxation time in ferrite cores. This concurs with work recently published by Mühlethaler, et al [10]. Additional plots this effect, as in Figure 12, but for different materials, are provided in Appendix C.

7 Degaussing

In Phase I, the apparatus was designed so that if sample cores had no initial magnetization, no residual magnetization would remain as a result of a measurement process. The process control sequence was

1. Set up and run the pulse timing logic signal (before turning on the bridge power supply; the function generator is always on).
2. Upload the required voltage to the bridge power supply.
3. Enable the power supply output.
4. After a delay, initiate the oscilloscope data acquisition sequence.
5. After the oscilloscope signals that data acquisition is complete, disable the power supply output; the voltage slews to zero at about 1.5 V/s. This slew rate is not programmable—it is just a property of the particular power supply we are using.
6. Delay several seconds to allow the power supply to settle and the core to cool.

However, there was some concern that there might still be some residual magnetization, either initially, in the core as supplied by the manufacturer, or introduced inadvertently, in the handling of the wound device, or due to an undiscovered defect in the apparatus or its control algorithm.

To check for this possibility, we created a degaussing control sequence, reran some experiments and compared the results with those obtained with the original setup. The new control sequence was

1. Setup and run the pulse timing logic signal.
2. Upload the *maximum* safe voltage to the bridge power supply and enable the power supply output. The voltage slews from zero to the maximum voltage, driving the core into saturation.
3. Upload the voltage required for the experiment. The output voltage slews down to that value at about 1.5 V/s. This is the degaussing step.
4. When the power supply output voltage reaches the correct value, initiate the oscilloscope data acquisition sequence.
5. After the oscilloscope signals that data acquisition is complete, disable the power supply output.
6. Delay for power supply settling and core cooling.

With this degaussing scheme, the residual flux for a square wave is limited to about $T^2 r/2$, where T is the period and r is the slew rate. At 10 kHz, this works out to about 8 nWb per turn.

This control sequence adds significantly to the overall run time for a sample, due to the degaussing voltage decay time. To speed things up, we switched from a worst-case, fixed delay (step 4 of the old sequence), to an adaptive delay that only waits long enough for the output voltage to reach its target.

Comparing the results we saw no significant difference. This makes us more confident, but it is not a conclusive result. A better approach might be to

institute degaussing on all runs, as a precautionary measure. There is a cost in run time, however. The additional delay for the degaussing step can add about three seconds per run, and samples typically require 200 to 300 runs.

8 Using the Data

The data that has been gathered in the project has been compiled in a distributions format that is available on DVD ROM and may be offered on a web site. Its format and interpretation is detailed in *Using the PSMA Rectangular Waveform Core Loss Data* [2], found in a PDF file in the data home directory. Briefly, the distribution has this directory structure:

`/` (The home directory.) General information, including the user manual, and indexes of cores and run sets.

`/cores/` Data files describing the various magnetic cores.

`/sets/` Containing subdirectories, each containing the data for a single run set and named for the set identifier, *`setId`*.

`/sets/`*`setId`*`/` Containing various data files describing the run set, and subdirectories with raw data and plots.

`/sets/`*`setId`*`/scope/` A directory containing the raw data from the oscilloscope: one CSV file for each run (characterized by frequency, peak voltage, and wave shape). There may be several hundred runs.

`/sets/`*`setId`*`/images/` Plots for each run, showing voltage, current, power, and energy, versus time.

`/sets/`*`setId`*`/auximages/` An optional directory, with more plots for special runs, such as those for the embedded winding experiments.

`/sets/`*`setId`*`/results/` Plots summarizing the runs set, comparing runs in families of curves. Appendix C describes the characterization plots, useful for design.

`/zips/` Zip archive files of the `/sets/` subdirectories, for ease of downloading.

Users browse the indexes found in the home directory, and select runs sets of interest. They can retrieve zip archive files of those run sets from the `/zips/` directory, or browse `/sets/`*`setId`*`/`, directly.

9 Future Work

Although this project has produced scientifically interesting new results and has developed techniques that are practical and useful to practicing engineers, many scientific questions and practical problems remain to be solved. In this section we outline some possibilities for future work.

9.1 Modeling

The model developed here provides improved accuracy in modeling core loss across a wide range of practical waveforms and frequencies. However, there are three important limits on its applicability:

- It does not account for the effects of DC flux bias in the core.
- It does not account for the off-time loss phenomenon.
- It provides a method for calculation of loss from a set of excitation waveforms, but does not provide a dynamic model applicable to simulation of a component, circuit, or system in a SPICE or other computer simulation.

Although there has been work published addressing the effects of DC bias and attempting to model the off-time loss phenomenon, it is not clear that the available approaches are practical or that they will work consistently across a wide range of excitation parameters, such as the data collected here. There is also a range of simulation models available for hysteretic behavior. However, most of these models address only static (rate-independent) hysteresis, and do not begin to capture the frequency and waveform dependence captured in the models and data we have developed. Work is needed on all three issues. The data collected in Phase II provides a rich resource for such work. For example, one would want to ensure that models developed provided results for the `hippo` waveform consistent with the data.

9.2 Hardware

Further hardware development may be considered for the purposes of developing capabilities beyond those of the equipment used in this work, and for developing equipment that is practical for routine square-wave core-loss measurement by core manufacturers and by core users.

The maximum frequency used in our testing was 500 kHz. Although applications at higher frequency are limited, rapid progress in wide-bandgap semiconductors is generating increased interest in switching frequencies in the MHz range. In addition, testing at higher frequencies could help ensure that the modeling provides accurate results for any waveform. Improvements in switching speed and stray impedances that would be needed to increase the frequency of operation would simultaneously increase the fidelity of waveforms and provide more accurate results near 500 kHz.

Now that the applicability of square-wave testing has been demonstrated, core manufacturers and by core users may wish to develop their own capability for this type of measurement. This calls for an easily replicable test setup using commercially available components, perhaps with some custom-made components.

9.3 Flux Spatial Dynamics

A small set of drilled-core measurements has shown that the flux distribution is not uniform across a core throughout a switching cycle. We hypothesize that the flux migration we see is consistent with the dimensional resonance effects analyzed in detail in [4]. In order to verify this, the dielectric constant of the material used needs to be measured. With this parameter, it would be possible to develop a simulation of expected behavior in the scenario we tested, to verify that what we observed can be attributed to this phenomenon. Another verification approach would be to repeat the drilled-core tests with sinusoidal excitation for which modeling is easier. If the behaviors do not agree, additional theoretical and experimental investigations would be called for.

Although [4] provides guidelines for determining when dimensional resonance effects become important, and approaches for calculating the effects when they are important, the analysis assumes sine-wave excitation. More work is needed to fully understand the implications of dimensional resonance effects with square-wave and other non-sinusoidal waveforms.

9.4 Design Implications

The most important implication of the data collection and modeling we performed for design work is that it is now possible to design a magnetic component and have fewer surprises about its loss behavior in a power electronics application. Having accurate models also allows employing computer optimization of designs.

Some of the design implications of the square wave loss data can be understood when the data is plotted in a Herbert plot as discussed in [11]. However, that discussion does not take into account the off-time loss phenomenon, or the different loss results obtained with the hippo waveform. Further work is needed to fully explore the design implications of these effects.

10 Conclusion

Together with the work in Phase I of this project, this work has greatly improved our understanding of core loss with non-sinusoidal waveforms. A key result is a simple approach to predict losses for various rectangular voltage waveforms. These calculations can be performed based on parameters we provide for materials we have measured, or can be based on simple square-wave measurements of other materials. An additional outcome of this work is a large data set of loss measurements for a wide variety of materials and waveforms that can be used for future study in this area.

A key component of this work was the evaluation of the composite waveform hypothesis, which allows analyzing the loss for various rectangular waveforms based on data taken for only square-wave excitation. This approach has been shown to be effective, and can be expected to give more accurate results than previous approaches.

Our detailed investigation of the composite waveform hypothesis uncovered a phenomenon in which the per-cycle losses increase with increasing "dead time" during which the core sits with a constant, elevated flux level. Further investigation of this has confirmed that it is a real effect, and it has generated international attention, with experiments by another group confirming the phenomenon we discovered. An approach to predicting loss including this effect has been proposed in [10]. Future work could develop better understanding of the phenomenon and easier approaches to predicting behavior considering it.

We also investigated the time dependence of the flux distribution through different regions of the core, both vertically and horizontally. We see transient oscillations of flux distribution that probably indicates the existence of standing waves due to low electromagnetic propagation velocity due to the high permeability and permittivity of the ferrite material. There is no indication that this is a significant loss mechanism for the experimental configuration, nor that it has any relevance for the dead-time loss anomalies.

This does not exclude the possibility that there are dynamic flux distribution effects at the micro or nano scale, but only shows that those we can detect on the scale of these experiments are not involved in a significant loss mechanism.

Three results of this work can readily be applied in practice. The first is predicting loss for any rectangular waveform using data from square-wave measurements. The second is using a two-plane Steinmetz model to fit this data over a wide frequency range. The third is the set of parameters for this model that we provide in Table 2 for the particular materials that we measured. An example and tutorial for using these parameters to predict loss with rectangular waveforms is provided in Appendix B.

Appendix

A Steinmetz Harmonic Analysis

In this appendix, we will examine core loss due to a square wave excitation voltage, as estimated by summing loss terms for the harmonics of the waveform, using the (sinusoidal) Steinmetz equation. Before beginning this analysis, it is useful to note that because of the nonlinear nature of the loss phenomena, one should not expect the Fourier approach to work well. We proceed with this analysis anyway to confirm the expectation that it will not work well. More discussion follows the analysis.

To examine calculate loss on the basis of the Fourier approach, we simply sum (7) over the harmonics, n:

$$\begin{aligned} \overline{P_v} &= \sum^{n} k f_n^{\alpha} \hat{B}_n^{\beta} \\ &= \sum^{n} k (nf)^{\alpha} \hat{B}_n^{\beta}. \end{aligned} \tag{17}$$

It is tempting to factor out k, α, and β, but they are somewhat dependant on frequency.

In our example, the Fourier series for our flux density, a triangle wave, is

$$B(t) = \frac{8\hat{B}}{\pi^2} \sum_{\text{odd}}^{n} \frac{(-1)^{(n-1/2)}}{n^2} \sin(2n\pi f t).$$

Using the Steinmetz model, we are only interested in the peak flux amplitude of each term, so we can simplify this to get

$$\hat{B}_n = \frac{8\hat{B}}{\pi^2 n^2}. \tag{18}$$

We then substitute this into (17),

$$\overline{P_v} = \sum_{\text{odd}}^{n} k (nf)^{\alpha} \left(\frac{8\hat{B}}{\pi^2 n^2} \right)^{\beta} \tag{19}$$

For a quantitative example, we will look at run `mi01-6-028`, which tests a Magnetics, div, Spang & Co. Inc. F material core (Table 3) at 125 kHz and $\hat{B} = 76\,\text{mT}$. The measured value of the core loss power density was $39\,\text{mW/cm}^3$. Using the Steinmetz harmonic analysis, we estimate the value at $28\,\text{mW/cm}^3$, low by 28%.

Parameter	Value for f above		
	0 kHz	100 kHz	500 kHz
k	0.074	0.036	0.014
α	1.43	1.64	1.84
β	2.85	2.68	2.28

Table 3: Published Steinmetz parameters for Magnetics Div., Spang & Co. R material [12]. Frequencies are referenced to 1 kHz, flux density to 1 kG, and $\overline{P_v}$ [=] mW/cm^2.

The failure of the harmonic analysis based on Fourier series to predict the loss accurately may be understood based on the nonlinear nature of the core loss. For linear phenomena such as resistive losses in windings or other conductors, in which loss is proportional to the square of the excitation amplitude, the loss calculated based on the Fourier decomposition can be mathematically proven to be identical to the loss calculated directly from the original waveform. However, this does not hold for a nonlinear system. Particularly in the lower end of the frequency range of interest, the Steinmetz parameters in Table 11 show that the power loss is proportional to the flux density to a power significantly greater than two, typically in the range of 2.4 to 3. On this basis, one can expect that when the full flux is considered together the loss will be higher than that that would be predicted based on the individual components considered separately. That is what we see in the results above.

Another experiment that illustrates the futility of using a Fourier decomposition to accurately predict core loss is described in [13]. A waveform consisting of a fundamental and a third harmonic is synthesized, and applied to a core under test. Varying the phase of the third harmonic has a significant effect on the loss. A Fourier decomposition could not capture this effect.

B Example Application

This section will demonstrate an example of using the two-plane Steinmetz fit parameters in Table 2 to calculate loss for an unusual waveform. The loss will be calculated using the conventional Steinmetz parameters of frequency and flux amplitude, and then the example will be repeated using voltage and pulse width as parameters. The design parameters for the example are shown in Table 4, and the waveform in Figure 16. The calculation of core loss would be identical whether this were an inductor or a transformer, and so we do not specify which. In the case of a transformer, there might be different numbers of turns and voltages on different windings, but the number of turns and corresponding voltage on any one winding would be adequate information.

B.1 Conventional Parameters

For the calculation based on frequency in flux density, we first calculate the amplitude of the flux density,

$$B_{\text{peak-to-peak}} = \frac{\int v dt}{NA} = \frac{5 \cdot 75 \text{ V}\mu\text{s}}{20 \cdot 154.8 \times 10^{-6} \text{ m}^2} = 0.12112 \text{ T} \tag{20}$$

$$\hat{B} = \frac{B_{peak-to-peak}}{2} = 0.06056 \text{ T} \tag{21}$$

Next, we need the square-wave loss for that flux amplitude, and for each of the pulse widths in the waveform: 5 μs and 7.5 μs. A square wave with a pulse width of 5 μs would have a period of 10 μs, and thus a frequency of 100 kHz. A square wave with a pulse width of 7.5 μs would have a period of 15 μs, and a frequency of 66.7 kHz. Based on the parameters in Table 2 for 3C90 material, we can calculate the square wave loss from (8). To do that, we calculate first with k_1, α_1, and β_1, and then again with k_2, α_2, and β_2, and we select the larger of the two calculated values. For example, at 100 kHz, for k_1, α_1, and β_1,

$$P_{v,1} = 36.86 \cdot (100 \times 10^3)^{1.19} \cdot (0.061)^{2.94} = 8819 \text{ W/m}^3 \tag{22}$$

The results for these calculations for each of the two frequencies and for each of the two parameter sets are shown in Table 5.

Parameter	Value
Core shape	PQ32/30
Core material	Ferroxcube 3C90
Effective core area, A	154.8 mm^2
Effective core volume	10.44 cm^3
Number of turns, N	20

Table 4: Example design parameters.

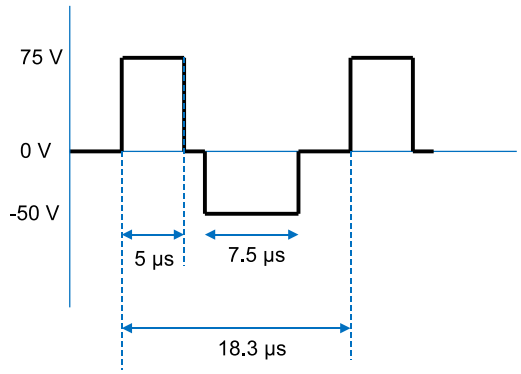

Figure 16: Example design voltage waveform applied across the winding of the device.

Plane	100 kHz	66.7 kHz
k_1, α_1, β_1	8.63 kW/m^3	5.33 kW/m^3
k_2, α_2, β_2	6.04 kW/m^3	2.29 kW/m^3

Table 5: Calculated square-wave loss.

From Table 5, we choose the maximum value in each column, to implement the maximum function in (8). In this case, the values in the first row of the table are the maxima for both frequencies.

We now have the square-wave power loss values, and in preparation for using the composite waveform hypothesis, we convert the form of these values to obtain the energy lost in each pulse. For the positive, 5 μs pulse, the energy loss is simply the pulse width multiplied by the corresponding power per unit volume: $E_a = 5\ \mu\text{s} \cdot 8.63\ \text{kW/m}^3 = 43.2\ \text{mJ/m}^3$ per pulse. Similarly, for the negative pulse, $E_b = 7.5\ \mu\text{s} \cdot 5.33\ \text{kW/m}^3 = 40.0\ \text{mJ/m}^3$. The total loss for cycle is the sum of the loss for each of these pulses, or 83.2 mJ/m^3. We can now convert that back to a power loss number by dividing by the total period, 18.3 μs, which results in a power per unit volume $P_v = 4.54$ kW/m^3. Based on the fact that kW/m^3 are the same as mW/cm^3, we can multiply that loss number by the volume in cm^3 to obtain the final power loss in milliwatts:

$$P = 4.64 \cdot 10.44 = 47.4\ \text{mW} \tag{23}$$

One can easily automate this calculation using Excel, Matlab, or any programming language, but it has been presented here in terms of the manual process in order to ensure that all the steps are clear without reference to any particular programming language.

B.2 Pulse width and Voltage as Parameters

In this case, we directly apply (11), repeated here for convenience:

$$E_{v,a} = \max\left(\frac{k_1}{(NA)^{\beta_1} 2^{(\beta_1+\alpha_1)}} V_a^{\beta_1} t_a^{\gamma_1} \ , \ \frac{k_2}{(NA)^{\beta_2} 2^{(\beta_2+\alpha_2)}} V_a^{\beta_2} t_a^{\gamma_2}\right) \tag{24}$$

We substitute in values from Table 4 and values of parameters $k_1 = 36.86$, $\alpha_1 = 1.19$, $beta_1 = 2.94$ and $\gamma_1 = 2.75$ for the first set and $k_2 = 2.895$, $\alpha_2 = 2.39$, $beta_2 = 2.16$ and $\gamma_2 = 2.77$ for the second. We obtain, for 5 μs and 75 V, $E_{v,a} = 43.2$ mJ/m^3, and, for 7.5 μs and 50 V, $E_{v,b} = 40.0$ mJ/m^3, exactly the same as was found with the other approach. Any difference would only occur as a result of roundoff errors tracking through the calculation.

As before, the total loss for cycle is the sum of the loss for each of these pulses, or 83.2 mJ/m^3. We can now convert that back to a power loss number by dividing by the total period, 18.3 μs, which results in a power per unit volume $P_v = 4.54$ kW/m^3, and an average power loss of 47.4 mW.

C Characterization Plots

Various plots have been provided with the data (Section 8) for visualizing the characterization (square wave) data. We present example plots in this appendix. For a more detailed explanation, see the user manual [2]. Image file names have the form *type*`conven-`*setId*`.`*ext*, where *type* is the type of plot, *setId* is the run set identifier, and `.`*ext* is the graphics file extension.

C.1 Conventional Core Loss Plots

Conventional plots of core loss versus $\hat{B}$ are provided. These are similar to the loss plots provided by manufacturers for sinusoidal excitation, but are for our square wave data.

Image file names have the form `conven-`*setId*`.`*ext*.

C.2 Herbert Curves

Herbert plots (Figure 17) show core loss versus pulse width, t_1, parameterized by $\hat{B}$. Herbert [3] describes their use in design.

Image file names have the form `conven-`*`setId.ext`*.

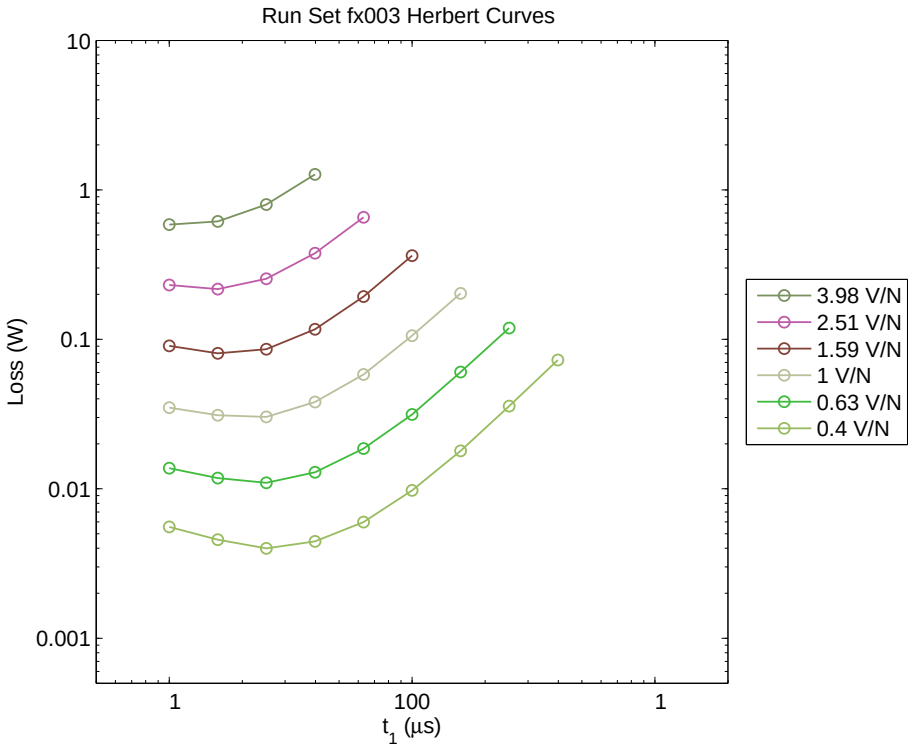

Figure 17: Herbert plot for Ferroxcube 3C81 material.

C.3 Hysteresis Plots

Hysteresis plots are provided for the characterisation square-wave data (Figure 18). The plots are presented in families of constant pulse width, varying $\hat{B}$. Because of ringing in the sense voltage signal due to limitation in the apparatus, simply plotting B versus H gives a messy plot, with the hysteresis loop shape obscured by the ringing. We use boxcar averaging, tuned to the ringing frequency (with a 85.3 μs window) to drop out the ringing. These plots do not have long saturation tails, partly because of this filtering, but also because the experiments did not generally drive the cores deep into saturation.

Image file names have the form `hyst-`*`setId`*`-`*`Tset`*`.`*`ext`*, where *`Tset`* is the pulse width family identifier.

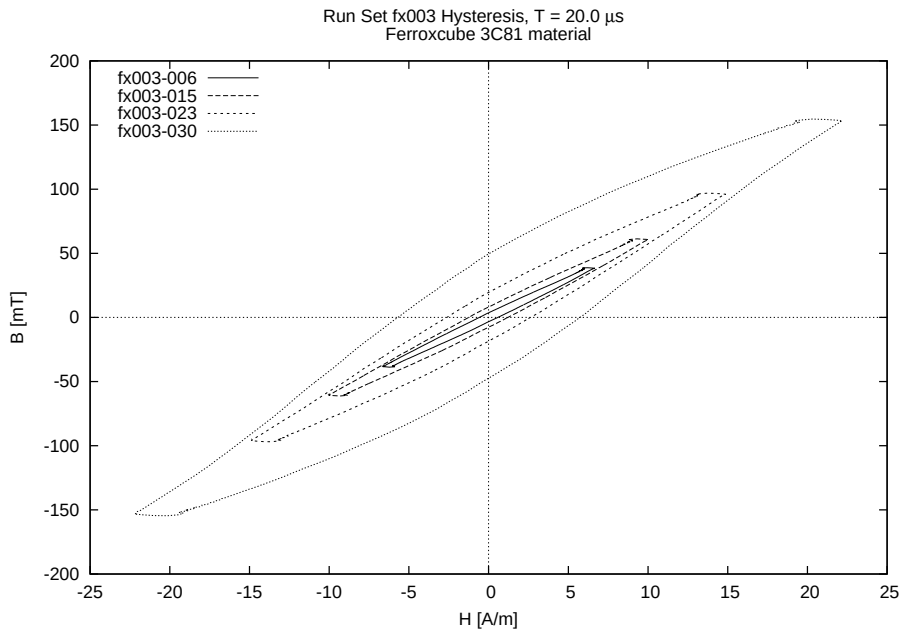

Figure 18: Hysteresis plot for Ferroxcube 3C81 material square wave data, 10 μs pulses. The legend gives the run identifiers, but these are not needed, as the only difference between the loops shown is the amplitude of excitation, and the value of $\hat{B}$ can be read from the plot.

D Expand Plots

In this appendix we present the `expand` waveform loss versus off-time plots for all the core materials tested.

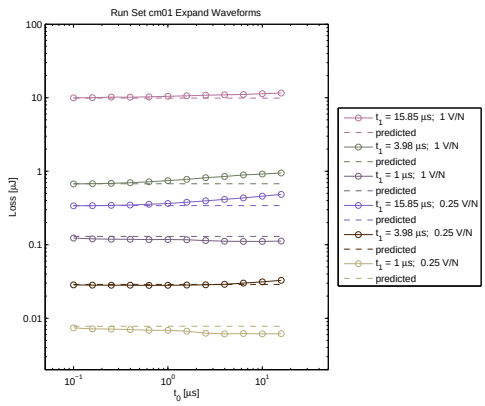

Figure 19: `expand` core loss vs. off-time for Ceramic Magnetics MN60.

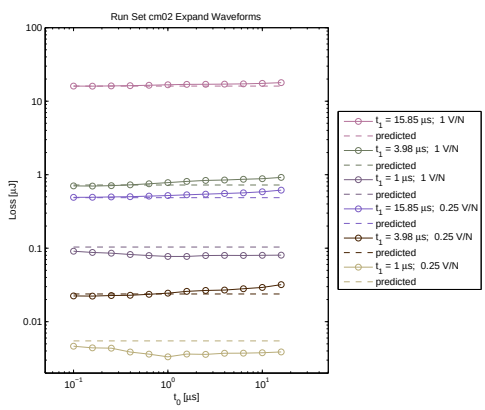

Figure 20: `expand` core loss vs. off-time for Ceramic Magnetics MN8CX.

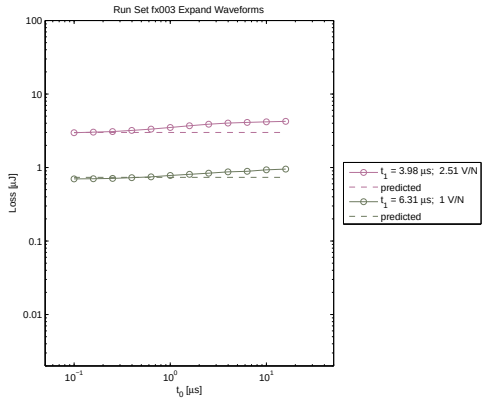

Figure 21: `expand` core loss vs. off-time for Ferroxcube 3C81.

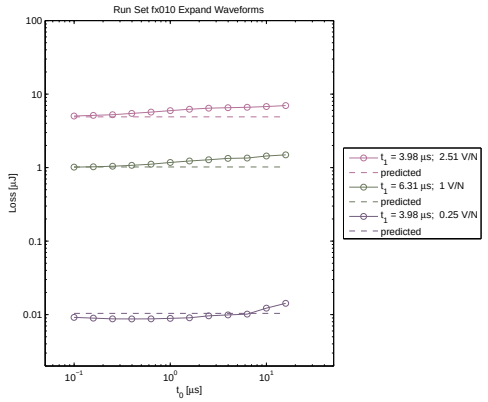

Figure 22: `expand` core loss vs. off-time for Ferroxcube 3C90.

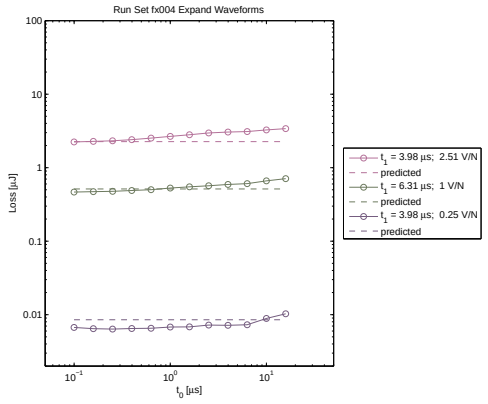

Figure 23: `expand` core loss vs. off-time for Ferroxcube 3F3.

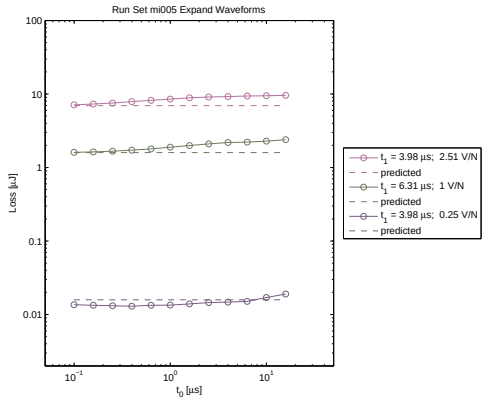

Figure 24: `expand` core loss vs. off-time for Magnetics F.

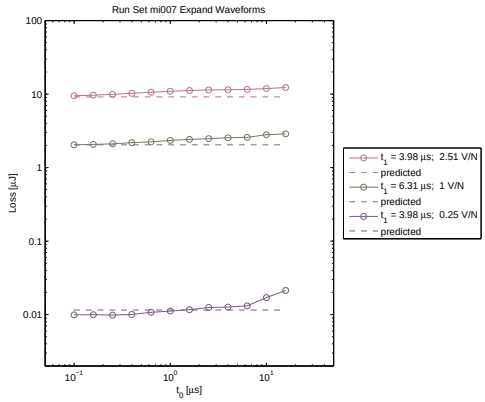

Figure 25: `expand` core loss vs. off-time for Magnetics K.

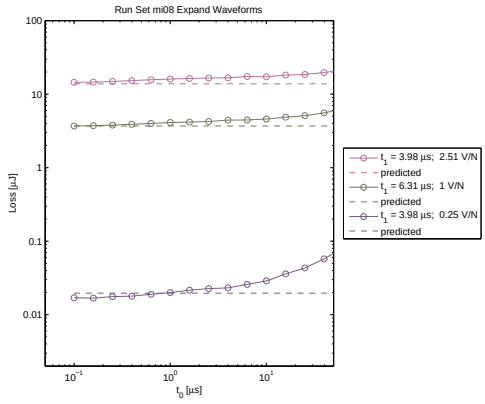

Figure 26: `expand` core loss vs. off-time for Magnetics L.

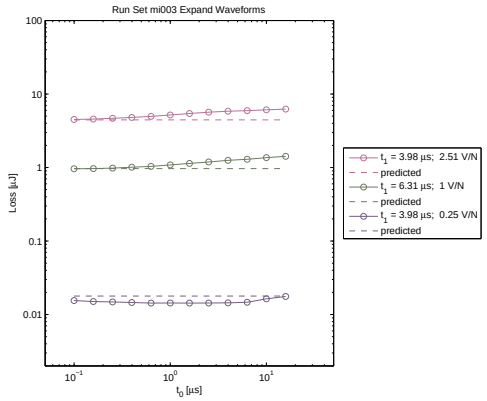

Figure 27: `expand` core loss vs. off-time for Magnetics P.

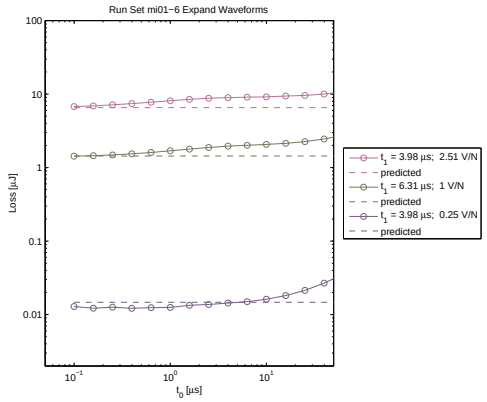

Figure 28: `expand` core loss vs. off-time for Magnetics R.

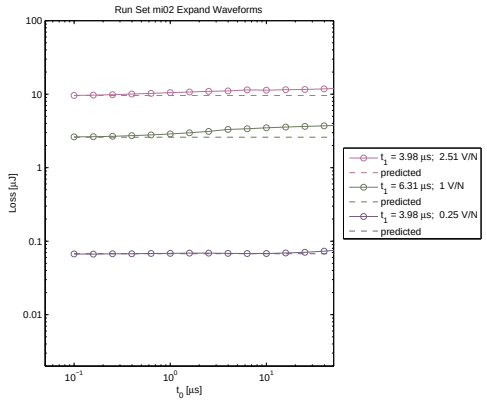

Figure 29: `expand` core loss vs. off-time for Magnetics W.

E Extended Steinmetz Table

In this appendix, we present Table 6, which is like Table 2, with the addition of the standard error of fit, in decibels, plus the parameters for additional run sets, including custom cores and nonstandard experiments for validating the apparatus.

Note:

1. The constriction experiment (Figure 4) comprised three run sets, starting with a Magnetics Inc. F42206-TC core, which was then modified by removing material to create a flux constriction.

2. Various other run sets used nonstandard procedures aimed at detecting problems with the apparatus that might explain the dead-time loss phenomenon (Section 6).

3. Run set `mi11-1` is the first of the drilled core experiments (Section 4), which all use the same core, `mi11`. Its effective area is somewhat less than the Magnetics Inc. 0F46113-TC core from which it was fabricated, due to the probe winding holes.

Manufacturer Material, shape (run set)	k_1 k_2	K_1 K_2	α_1 α_2	β_1 β_2	Std err Note
Ceramic Magnetics Inc					
MN60, 23.2,14.5,7.2T (cm01)	6.085	86810	1.32	2.47	0.33 dB
	899.8μ	67879	2.00	2.13	
MN8CX, 23.2,15.1,7.7T (cm02)	63.01	182100	1.19	2.49	0.32 dB
	177.4μ	87357	2.20	2.29	
Ferroxcube					
3C81, TX22/14/13 (fx003)	11.01	91200	1.31	2.61	0.34 dB
	65.32μ	41432	2.18	2.11	
3C81, E19/8/5 (fx09)	18.02	88800	1.23	2.45	0.46 dB
	350.0μ	52769	2.10	2.33	
3C90, TX22/14/6.4 (fx010)	36.86	39570	1.19	2.94	0.44 dB
	2.895μ	18223	2.39	2.16	
3F3, TX22/14/13 (fx004)	102.4	67200	1.13	2.81	0.48 dB
	11.93μ	28414	2.30	2.14	
3F3, E19/8/5 (fx05)	40.63	65950	1.14	2.50	0.44 dB
	224.8μ	38221	2.12	2.36	
Magnetics Inc.					
F, 42206-TC (mi005)	26.41	72920	1.24	2.76	0.40 dB
	7.612μ	32369	2.37	2.22	note 2
F, 46113-TC (mi11-1)	142.9	63340	1.02	2.43	0.49 dB
	6.299μ	28835	2.35	2.11	note 3
K, 42206-TC (mi007)	246.2	86830	1.10	2.95	0.55 dB
	5.276μ	20750	2.41	2.48	
L, 2206 (mi08)	706.8	150800	1.04	2.87	0.96 dB
	276.1m	99927	1.69	2.88	
P, 42206-TC (mi003)	10.91	43090	1.28	2.80	0.37 dB
	75.99μ	36099	2.16	2.13	
R, 42206-TC (mi01-2)	12.39k	36760	0.83	3.65	1.84 dB
	18.21m	68202	1.75	2.15	
R, custom (mi009)	148.9k	6237	0.71	4.90	1.48 dB
	1.796	100162	1.39	2.18	note 1
R, 42206-TC (mi01-1)	29.19k	38530	0.69	3.34	1.61 dB
	124.2m	77954	1.59	2.16	note 1
R, custom (mi010)	68.73k	28710	0.71	3.92	1.14 dB
	423.7m	90425	1.50	2.17	note 1
R, 42206-TC (mi01-3)	38.01	65250	1.24	2.99	0.40 dB
	40.00μ	31023	2.21	2.16	note 2
R, 42206-TC (mi01-4)	38.72	121900	1.19	2.44	0.34 dB
	8.618m	65931	1.84	2.31	note 2
R, 42206-TC (mi01-5)	44.61	68680	1.22	2.92	0.40 dB
	18.93μ	27996	2.28	2.21	note 2
R, 42206-TC (mi01-6)	30.16	67220	1.25	2.90	0.36 dB
	14.55μ	30033	2.31	2.24	note 2
W, 42206-TC (mi02)	832.7m	131000	1.51	2.37	0.19 dB
	10.59m	123857	1.82	2.04	

Table 6: More two-plane Steinmetz parameters including custom cores and nonstandard experiments. The k_i parameters are referenced to $f = 1\,\mathrm{Hz}$ and $\hat{B} = 1\,\mathrm{T}$; the K_i parameters are referenced to $f = 100\,\mathrm{kHz}$ and $\hat{B} = 100\,\mathrm{mT}$. All the k_i and K_i parameter have dimensions of $\mathrm{W/m^2}$. The notes are explained in the text.

Acknowledgements

We thank the Power Sources Manufacturers Association and the National Institute for Standards and Technology (NIST) for support of this work.

References

[1] Charles R. Sullivan and John H. Harris. Testing core loss for rectangular waveforms, phase I final report. Technical report, Power Sources Manfacturers Association, 2010. Available at `http://www.psma.com/sites/default/files/Sullivan\%20Core\%20Loss\%20Report\%200207101.pdf`.

[2] Charles R. Sullivan and John H. Harris. *Using the PSMA Rectangular Waveform Core Loss Data*. Power Sources Manfacturers Association, 2011.

[3] Edward Herbert. User-friendly data for magnetic core loss calculations. Unpublished., August 2008.

[4] Glen R. Skutt. *High-Frequency Dimensional Effects in Ferrite-Core Magnetic Devices*. PhD thesis, Virginia Polytechnic Institute and State University, 1996.

[5] Ferrite material selection guide, 2000. Magnetics Division of Spang & Company, Bulletin No. FC-S1.

[6] Soft ferrites and accessories, data handbook, 2009. Ferroxcube, Eindhoven, The Netherlands.

[7] C. P. Steinmetz. On the law of hysteresis. *AIEE Transactions*, 9:3–64, 1892. Reprinted under the title "A Steinmetz contribution to the ac power revolution", introduction by J. E. Brittain, in *Proceedings of the IEEE* 72(2) 1984, pp. 196–221.

[8] E. C. Snelling. *Soft Ferrites, Properties and Applications*. Butterworths, second edition, 1988.

[9] K. Venkatachalam, C. R. Sullivan, T. Abdallah, and H. Tacca. Accurate prediction of ferrite core loss with nonsinusoidal waveforms using only Steinmetz parameters. In *IEEE Workshop on Computers in Power Electronics*, 2002.

[10] J. Mühlethaler, J. Biela, J. W. Kolar, and A. Ecklebe. Improved core loss calculation for magnetic components employed in power electronic systems. In *Proceedings of APEC 2011—Applied Power Electronics Conference and Exposition*, pages 1729–36, 2011.

[11] Charles R. Sullivan, John H. Harris, and Edward Herbert. Core loss predictions for general PWM waveforms from a simplified set of measured data. In *Applied Power Electronics Conference and Exposition (APEC), 2010 25th Annual IEEE*, pages 1048–1055, February 2010.

[12] Curve fit equations for ferrite materials, 1999. Magnetics Division of Spang & Company, Bulletin No. FC-S7.

[13] Jieli Li, T. Abdallah, and C. R. Sullivan. Improved calculation of core loss with nonsinusoidal waveforms. In *IEEE Industry Applications Society Annual Meeting*, pages 2203–2210, 2001.